

Inferring Hidden Symmetries of Exotic Magnets from Learning Explicit Order Parameters

Nihal Rao,^{1,2} Ke Liu,^{1,2,*} and Lode Pollet^{1,2,3}

¹*Arnold Sommerfeld Center for Theoretical Physics,
University of Munich, Theresienstr. 37, 80333 München, Germany*

²*Munich Center for Quantum Science and Technology (MCQST), Schellingstr. 4, 80799 München, Germany*

³*Wilczek Quantum Center, School of Physics and Astronomy,
Shanghai Jiao Tong University, Shanghai 200240, China*

(Dated: June 10, 2022)

An unconventional magnet may be mapped onto a simple ferromagnet by the existence of a high-symmetry point. Knowledge of conventional ferromagnetic systems may then be carried over to provide insight into more complex orders. Here we demonstrate how an unsupervised and interpretable machine-learning approach can be used to search for potential high-symmetry points in unconventional magnets without any prior knowledge of the system. The method is applied to the Heisenberg-Kitaev model on a honeycomb lattice, where our machine learns the transformations that manifest its hidden $O(3)$ symmetry, without using data of these high-symmetry points. Moreover, we clarify that, in contrast to the stripy and zigzag orders, a set of D_2 and D_{2h} ordering matrices provides a more complete description of the magnetization in the Heisenberg-Kitaev model. In addition, our machine also learns the local constraints at the phase boundaries, which manifest a subdimensional symmetry. This work highlights the importance of explicit order parameters to many-body spin systems and the property of interpretability for the physical application of machine-learning techniques.

I. INTRODUCTION

Applications of machine learning in different fields of physics have become ubiquitous and witnessed a dramatic rise in the past few years [1, 2], ranging from statistical physics [3, 4], condensed matter physics [5–7], chemistry and material science [8–10], to high energy physics [11–13] and quantum computation [14–16]. Although studies in the earlier stages have primarily focused on benchmarking algorithms, many recent developments are moving towards practical tools for solving more complicated and challenging problems. Instances of these advances include, for example, discovering new classes of wavefunctions in strongly-correlated systems [17], improving the accuracy on atoms and small molecules [18, 19], designing efficient algorithms [20–22], and analyzing experiments [23–25].

Here we explore the potential of using machine-learning techniques to search for hidden symmetries in many-body spin systems. Symmetry is at the heart of our understanding of physics. Apparent symmetries such as time, spatial, and rotational invariance lead to the conservation of energy, momentum, and angular momentum, respectively. However, quite often, the effective symmetry of a system is not apparent, which we henceforth refer to as hidden symmetry. For instance, in some extended Kitaev systems, which are subject to active research due to their proximity to Kitaev spin liquids [26] and other exotic phases [27–31], there exist high-symmetry points. At these points, a complex ordering pattern

may be transformed to a simple one [32–34]. Knowledge of conventional orders can then be carried over, and pseudo-Goldstone modes may be realized even when the Hamiltonian seemingly manifests a low discrete symmetry. Others remarkable examples are the Bethe-ansatz solvable $SU(3)$ point in the spin-1 bilinear-biquadratic chain [35–38] and the emergent $O(4)$ symmetry in the spin-1/2 J - Q model [39].

Although hidden symmetries are of broad relevance and rich in physics, identifying them is a non-trivial task and is very much problem-dependent, often requiring remarkable insights and experience from researchers. Therefore, it would be interesting and useful if machine-learning techniques can facilitate their identification.

In this paper, we show that the tensorial-kernel support vector machine (TK-SVM) [40–42], which is an *unsupervised* and *interpretable* machine-learning method, provides an efficient and versatile approach to detect high symmetry points hidden in unconventional magnets. We demonstrate the method by applying it to the honeycomb Heisenberg-Kitaev (HK) model, where our machine correctly identifies its hidden $O(3)$ symmetries and the associated transformations. Moreover, we clarify that the pictorial description of the zigzag and stripy orders only partially reflect the ordering in the HK model. The complete orders are characterized by a set of D_2 and D_{2h} ordering matrices.

The paper is organized as follows. In Section II we define the HK Hamiltonian and review the TK-SVM method. Section III discusses the machine-learned phase diagram. Section IV is devoted to explicit order parameters and the corresponding magnetization curves. The connection between hidden symmetries and ordering matrices is given in Section V. Section VI provide a discus-

* ke.liu@lmu.de

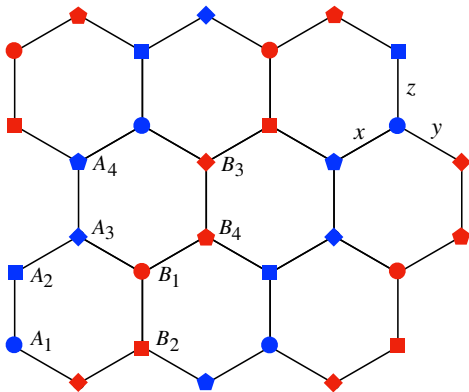


FIG. 1. Depiction of the a honeycomb lattice and the D_{2h} and D_2 magnetic cell, which contain eight spins and two sectors marked by A (blue) and B (red). This choice of magnetic cell fits zigzag and stripy patterns along different directions and also applies to states at the hidden $O(3)$ points which cannot be captured by a four-site zigzag or stripy cell. x, y, z label the three distinct bonds in the Kitaev interaction.

sion of local constraints and a subdimensional symmetry at phase boundaries. We conclude in Section VII with an outlook.

II. MODEL AND METHOD

We consider the HK model on a honeycomb lattice to demonstrate the concept. It should be noted however that the following discussion is intended to provide a general guidance for using TK-SVM to search for unconventional orders and hidden symmetries, and is transferable to other spin systems.

A. Heisenberg-Kitaev Hamiltonian

The honeycomb HK model is defined as

$$H = \sum_{\langle ij \rangle_\gamma} J \vec{S}_i \cdot \vec{S}_j + K S_i^\gamma S_j^\gamma, \quad (1)$$

where J and K denote the Heisenberg and Kitaev interaction, respectively, and can be parameterized by an angle variable $\varphi \in [0, 2\pi)$ with $K = \sin \varphi$, $J = \cos \varphi$; $\gamma \in \{x, y, z\}$ labels the three types of nearest-neighboring bonds $\langle ij \rangle_\gamma$, as depicted in Figure 1.

The Hamiltonian Eq. (1) is a candidate model of Kitaev materials [27–30] and hosts four magnetic orders and two Kitaev spin liquids (KSLs) [28, 33, 43, 44].

B. TK-SVM

The TK-SVM is an interpretable and unsupervised approach to detect general symmetry-breaking spin orders [40, 41] and emergent local constraints [42, 45]. It

is formulated in terms of the decision function

$$d(\mathbf{x}) = \sum_{\mu\nu} C_{\mu\nu} \phi_\mu(\mathbf{x}) \phi_\nu(\mathbf{x}) - \rho. \quad (2)$$

Here, $\mathbf{x} = \{S_i^a | a = x, y, z; i = 1, 2, \dots, N\}$ denotes configurations of N spins and serves as training data. $\phi_\mu(\mathbf{x})$ maps \mathbf{x} to a tensorial feature space, the ϕ -space, which can represent general spin orders, regardless of exotic magnets, tensorial nematics [40, 41] and emergent local constraints for spin liquids [42, 45]. $C_{\mu\nu}$ can be viewed as an encoder of order parameters, from which explicit expressions of the detected orders are identified. ρ is a bias parameter probing whether two sample sets originate from the same phase. See Appendix A for details.

Although the decision function Eq. (2) carries out a binary classification between two sets of data, TK-SVM can also classify multiple data sets. Such a multi-classification is essentially realized by individual binary problems but makes it possible to compute a phase diagram via unsupervised graph partitioning.

Consider a spin Hamiltonian characterized by a number of physical parameters, such as temperature and different kinds of interactions. We can cover its parameters space, \mathcal{V} , by a grid of the same dimensionality. The choice of the grid is arbitrary, either uniform or distorted to have denser nodes in the most interesting subregions of \mathcal{V} . We collect spin configurations \mathbf{x} at vertices of the grid and perform the SVM multi-classification on the sampled data. For a grid of M vertices, this will produce $M(M-1)/2$ decision functions as Eq. (2), comprising of binary classifications between each pair of vertices. We then introduce a weighted edge between two vertices, and the weight, $w(\rho) \in [0, 1]$, is based on the bias parameter in the corresponding $d(x)$. In this way, we create a graph with M vertices and $M(M-1)/2$ edges; its partitioning will give the phase diagram.

In formal terms, the graph can be described by a M -by- M Laplacian matrix \hat{L} . The off-diagonal entries of \hat{L} accommodate edge weights connecting vertices, and the diagonal entries are degrees of those vertices. The partitioning can be solved by Fiedler's theory of spectral clustering [46, 47],

$$\hat{L} \mathbf{f}_i = \lambda_i \mathbf{f}_i. \quad (3)$$

The second smallest eigenvalue λ_2 measures the algebraic connectivity of the graph. The corresponding eigenvector \mathbf{f}_2 is referred as the *Fiedler vector*, which reflects how the vertices are clustered and plays the role of a phase diagram in the context of TK-SVM [41, 42]. We refer to Appendix B for details.

III. MACHINE-LEARNED PHASE DIAGRAM

A typical application of TK-SVM consists of two steps: (i) detecting the topology of the phase diagram, (ii) extracting and verifying order parameters. We focus here

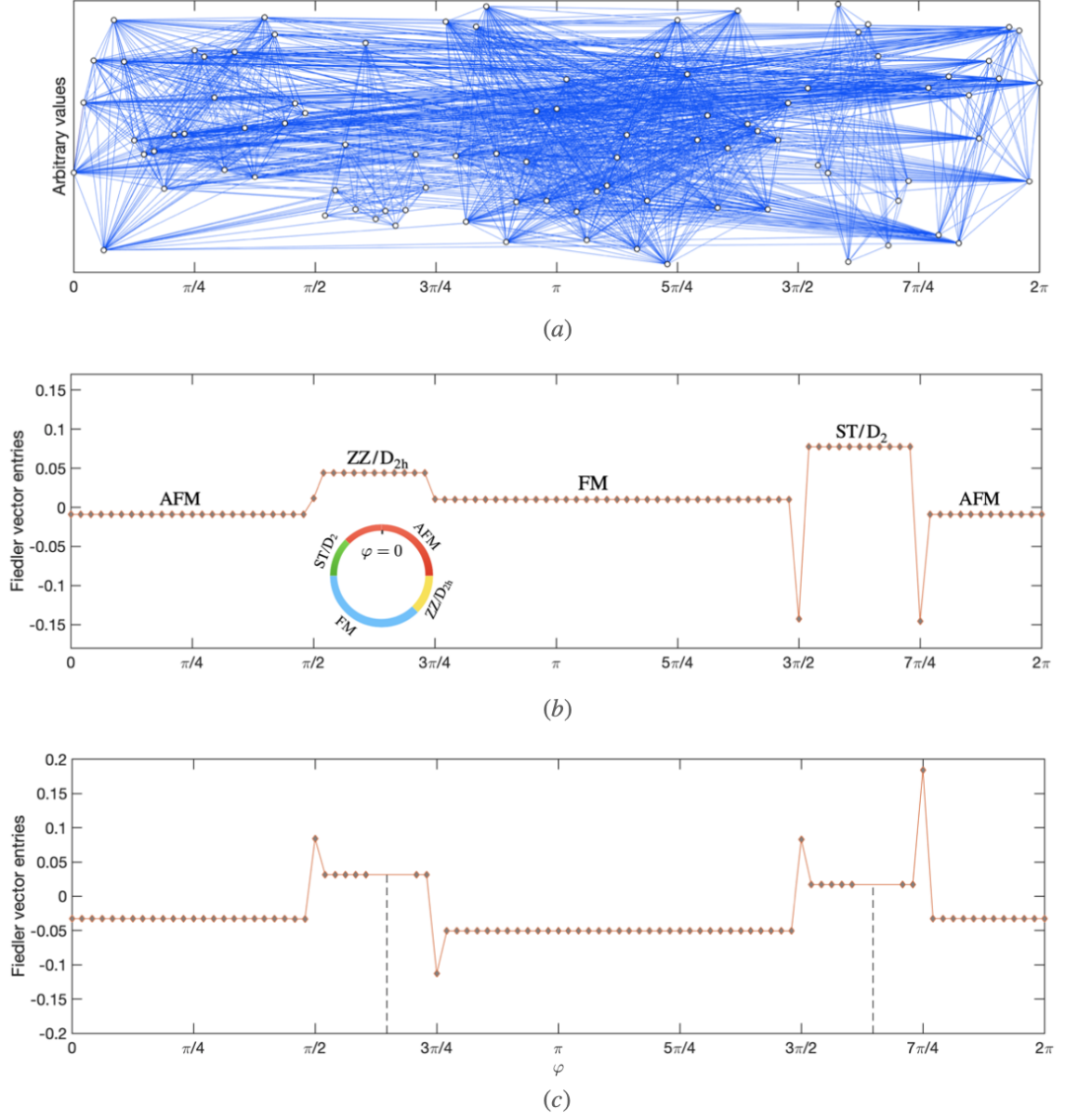


FIG. 2. Machine-learned phase diagram of the Heisenberg-Kitaev model. (a) A fully-connected graph of 96 vertices (white cycles) and 4,560 edges (blue lines). Each vertex represents a value of φ . The edges are weighted according to biases ρ learned in a rank-1 TK-SVM multi-classification (cf. Section III and Appendix B for details). Since the parameter space is one-dimensional, a second dimension is introduced with arbitrary values to avoid the edges from overlapping in this representation. (b) The Fiedler vector obtained from partitioning the graph. Each entry corresponds to a vertex, while gradients in their value reflect the clustering of the graph. The plateaus indicate stable phases, and the jumps signal phase transitions. The phases are interpreted in Section IV and are labelled following the common convention: AFM, antiferromagnet; ZZ, zigzag; FM, ferromagnet; ST, stripy. In addition, the ST and ZZ region are also marked according to the D_2 and D_{2h} magnetization measured in Figure 4. The inner panel shows a circular representation of the phase diagram. (c) Another partitioning with removing data near the high-symmetry points $\varphi = \arctan(-2) \sim 0.65\pi, 1.65\pi$ (indicated by the dashed lines; the graph is not shown), to demonstrate that data of these special points is not needed for revealing the hidden $O(3)$ symmetry. The partitioning is reflected by contrasts between Fiedler-vector entries, rather than the absolute values. Panels (a) and (c) lead to the same topology of the phase diagram.

on the classical phase diagram of the HK model Eq. (1), and save the discussion of order parameters for the next section.

For this purpose, we introduce a fictitious grid that

spans uniformly in the space of φ , with a spacing of $\delta\varphi = \frac{\pi}{48}$. At each φ , we collect 500 spin configurations at a low temperature $T = 10^{-3}\sqrt{J^2 + K^2}$. The samples are prepared by classical parallel tempering Monte Carlo

| Phases | Ordering Matrices |
|----------|---|
| D_2 | $T_1^{A,B} = \begin{pmatrix} 1 & 0 & 0 \\ 0 & 1 & 0 \\ 0 & 0 & 1 \end{pmatrix}, \quad T_2^{A,B} = \begin{pmatrix} -1 & 0 & 0 \\ 0 & -1 & 0 \\ 0 & 0 & 1 \end{pmatrix},$ $T_3^{A,B} = \begin{pmatrix} -1 & 0 & 0 \\ 0 & 1 & 0 \\ 0 & 0 & -1 \end{pmatrix}, \quad T_4^{A,B} = \begin{pmatrix} 1 & 0 & 0 \\ 0 & -1 & 0 \\ 0 & 0 & -1 \end{pmatrix}$ |
| D_{2h} | $T_1^{A,B} = \pm \begin{pmatrix} 1 & 0 & 0 \\ 0 & 1 & 0 \\ 0 & 0 & 1 \end{pmatrix}, \quad T_2^{A,B} = \pm \begin{pmatrix} 1 & 0 & 0 \\ 0 & 1 & 0 \\ 0 & 0 & -1 \end{pmatrix},$ $T_3^{A,B} = \pm \begin{pmatrix} -1 & 0 & 0 \\ 0 & 1 & 0 \\ 0 & 0 & -1 \end{pmatrix}, \quad T_4^{A,B} = \pm \begin{pmatrix} -1 & 0 & 0 \\ 0 & 1 & 0 \\ 0 & 0 & 1 \end{pmatrix}$ |

TABLE I. D_2 and D_{2h} ordering matrices. Their magnetic cells are shown in Figure 1, which consist of two sublattice sectors, labeled by A, B . The D_2 and D_{2h} orders involve four and eight distinct matrices, respectively, forming the respective three-dimensional dihedral groups. Their ordering matrices also define the sublattice transformations that identify the hidden $O(3)$ points in the Heisenberg-Kitaev model.

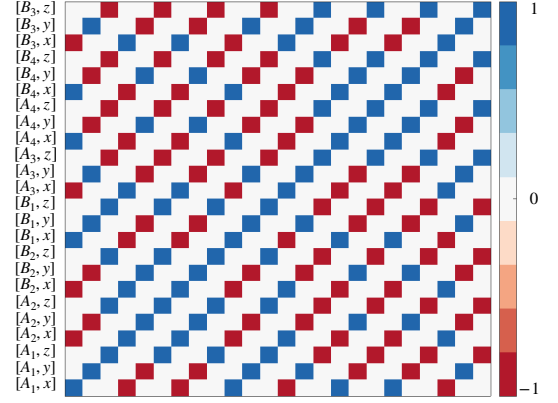
(PTMC) simulations on a lattice of 10,368 spins (72×72 honeycomb unit cells). Next, we perform TK-SVM with different ranks over these data. However, it turns out that a rank-1 TK-SVM (cf. Appendix A), which detects magnetic orders, is sufficient to learn the phase diagram. The result is a graph of 96 vertices and 4,560 edges as shown in Figure 2 (a).

The Fiedler vector obtained from partitioning the graph is depicted in Figure 2 (b) (see also Appendix B). Each of its entry represents a vertex of the grid, hence a φ -point. The Fiedler-vector entries for the vertices (φ s) classified in the same subgraph component are identical or very close in value, while those falling into different subgraphs display considerable contrast.

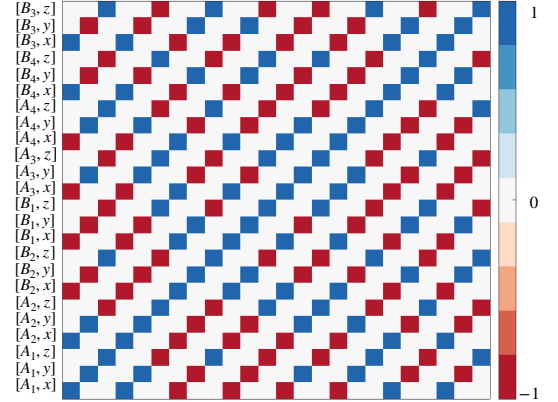
Evidently, the Fiedler vector shows four subgraph components, indicating four stable phases. This in fact reproduces the classical HK phase diagram [43, 44]. The four plateaus respectively correspond to the antiferromagnetic (AFM), zigzag (ZZ), ferromagnetic (FM) and stripy (ST) phase, following the labeling in Figure 2 (b). However, as we shall discuss in Section IV, orders in the regions $\varphi \in (\frac{\pi}{2}, \frac{3\pi}{4})$ and $(\frac{3\pi}{2}, \frac{7\pi}{4})$ may be more universally measured by D_2 and D_{2h} magnetization.

Sudden jumps in the Fiedler vector entries manifest phase transitions, which are seen to occur at $J = 0$, $K = \pm 1$ ($\varphi = \frac{\pi}{2}, \frac{3\pi}{2}$) and $J = -K$ ($\varphi = \frac{3\pi}{4}, \frac{7\pi}{4}$). The boundaries at $K = \pm 1$ correspond to the Kitaev limits. Different from the cases of quantum spin-1/2 and spin-1, where KSLs are proposed to extend to finite regions of J [28, 33, 48–51], in the large- S limit, KSLs are unstable against the Heisenberg interaction and reduce to critical points. Nevertheless, this will not affect our discussion of the hidden symmetries in the HK model.

We note that the learning of Figure 2 is unsupervised. No prior knowledge of the phase diagram and order parameters were used. Moreover, all the four phases are discriminated simultaneously by a *single* partitioning.



(a) D_2



(b) D_{2h}

FIG. 3. The $C_{\mu\nu}$ matrices learned by a rank-1 TK-SVM in the ST/ D_2 and ZZ/ D_{2h} phases. Each entry represents a correlation between two spin components defined by the weighted sum of the support vectors (Appendix A). Results of an eight-spin cluster (2×2 honeycomb unit cells), which is the minimal unit of the D_2 and D_{2h} order, are shown for demonstration. From bottom to top, the vertical axis is labeled in the same convention as in the lattice Figure 1. The same labeling applies to the horizontal axis from left to right. The interpretation of these patterns leads to the respective ordering matrices in Table I.

IV. EXPLICIT ORDER PARAMETERS

We move on to interpret the nature of the phases shown in the phase diagram of Figure 2. By virtue of the strong interpretability, analytical order parameters can be extracted from the corresponding $C_{\mu\nu}$ matrix. As the FM and AFM orders are trivial, we will focus on the other two phases.

The $C_{\mu\nu}$ matrices learned in the ST/ D_2 and ZZ/ D_{2h} phases are shown in Figure 3. Each entry is an indication for the correlation between two spin components. The alternating colors indicate sign flips on individual spin components, rather than entire spins. The interpretation of each $C_{\mu\nu}$ can be summarized by a set of ordering matrices shown in Table I. The respective magnetization

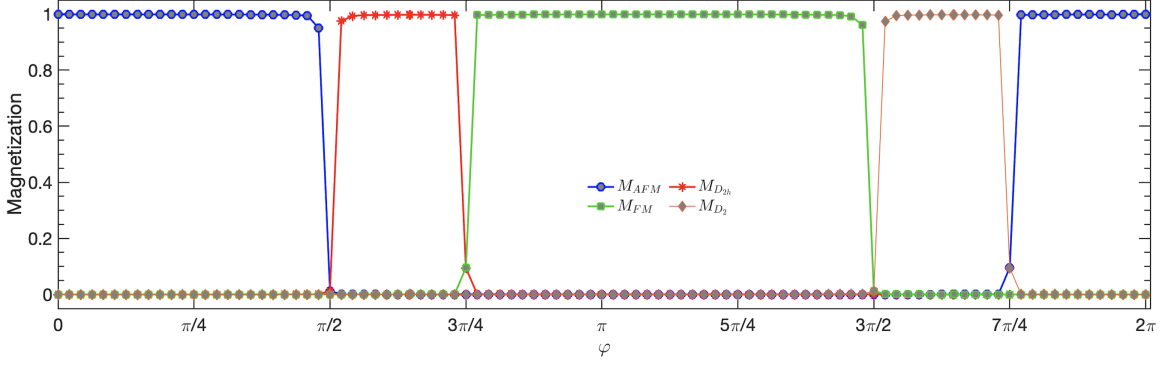


FIG. 4. Measurements of order parameters. The FM, AFM, D_2 and D_{2h} magnetization are measured as a function of φ at low temperature $T = 10^{-3}\sqrt{J^2 + K^2}$. In each phase, the respective magnetization saturates to unity ($M = \langle |\frac{1}{N_{\text{cell}}} \sum_{\text{cell}} \vec{M}| \rangle = 1$), while others vanish, where \vec{M} is the ordering moment in one magnetic cell, \sum_{cell} sums over magnetic cells, and $\langle \dots \rangle$ denotes the ensemble average. The small residual moments at $\varphi = 0.75\pi, 1.75\pi$ are a finite-size effect (FSZ). At these points, the classical ground states form decoupled FM and AFM Ising chains with a subextensive degeneracy (Section VI).

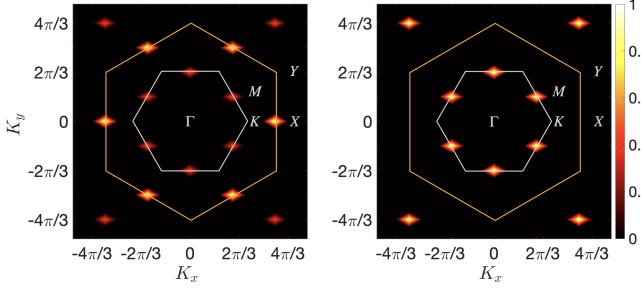


FIG. 5. Static spin-structure factor, $S(\vec{K})$, for the ST and D_2 (left) and ZZ and D_{2h} order (right). The orange and grey hexagon denote the second and first honeycomb Brillouin zone respectively, and high symmetry points are indicated. $S(\vec{K}) = \langle \frac{1}{N} \sum_{ij} \vec{S}_i \cdot \vec{S}_j e^{i\vec{K} \cdot (\vec{r}_i - \vec{r}_j)} \rangle$, where \vec{r}_i is the position of a spin at site i , and a nearest-neighbor bond of the honeycomb lattice is set to unit length.

is expressed as

$$\vec{M} = \frac{1}{8} \sum_{A,B} \sum_{k=1}^4 T_k^{A,B} \vec{S}_k, \quad (4)$$

where $T_k^{A,B}$ are ordering matrices, and A, B denote the two sublattice sectors indicated in Figure 1.

The D_2 order is formulated by four different matrices with $T_k^A = T_k^B$, forming the three-dimensional dihedral group D_2 . (The numeration of spins in the A and B sector is nevertheless different.) These matrices have been proposed in the study of orbital degeneracy of Mott insulators [52, 53] and are used to identify the hidden symmetries of the HK model [28, 32], which will be discussed in Section V. The D_{2h} order can be viewed as an AFM version of the D_2 order, where $T_k^A = -T_k^B$ in the respective sublattice. It is thereby aptly named after the dihedral group $D_{2h} \cong D_2 \times Z_2$.

These order parameters, as well as the FM and Neel orders, are measured at $T = 10^{-3}\sqrt{J^2 + K^2}$ which is the

temperature during training the TK-SVM. As shown in Figure 4, the respective magnetization saturates to unity, spans the entire phase, and vanishes in the other phases.

The measurements of D_{2h} and D_2 magnetization validate that they are the correct order parameters for the regions $\varphi \in (\frac{\pi}{2}, \frac{3\pi}{4})$ and $(\frac{3\pi}{2}, \frac{7\pi}{4})$. These regions are traditionally described by zigzag and stripy orders [43, 44, 54], which have the same static structure factor as the D_{2h} and D_2 order as shown in Figure 5. We now discuss the relation and differences between these orders.

Figure 6 shows configurations of a D_{2h} and a D_2 state, which can be generated by fixing one spin, e.g. $\vec{S}_{A_1} = \vec{S}_0$, and determining the orientation of other spins according to the respective ordering matrices in Table I. In general, the reference spin \vec{S}_0 may point along any direction. However, there are special instances where the D_{2h} and D_2 structures can reduce to the zigzag and stripy orders respectively. For example, the case $\vec{S}_0 = (0 \ 0 \ \pm 1)^T$ reduces to the Z-type zigzag and stripy state as shown in Figure 7. Similarly, choosing $\vec{S}_0 = (\pm 1 \ 0 \ 0)^T$ and $(0 \ \pm 1 \ 0)^T$ will lead to an X- and Y-type zigzag and stripy state, respectively. Namely, the manifolds of the zigzag (stripy) and D_{2h} (D_2) order have overlaps.

In the ZZ/ D_{2h} and ST/ D_2 regions, away from the hidden symmetry ($O(3)$) points at $\varphi \approx 0.65\pi, 1.65\pi$, the above special states are realized as the ground states of the HK model owing to the discrete symmetry of the Kitaev term; as visualized in Figure 8. For these states, the distinction between D_{2h} (D_2) and zigzag (stripy) orders is superfluous. Nevertheless, once spins are unlocked from the axes, which happen at the $O(3)$ points, the states can no longer be described by staggered arrangements of $\pm \vec{S}$ as in a zigzag or stripy structure.

Consider a Z-type zigzag (stripy) moment for instance. As measured in Figure 9, its expectation value at the $O(3)$ point is $M = \frac{1}{2}$ when $T \rightarrow 0$. This can be understood by parametrizing the reference spin as $\vec{S}_0 = (\sin \theta \sin \phi \ \sin \theta \cos \phi \ \cos \theta)^T$, where θ, ϕ are Euler an-

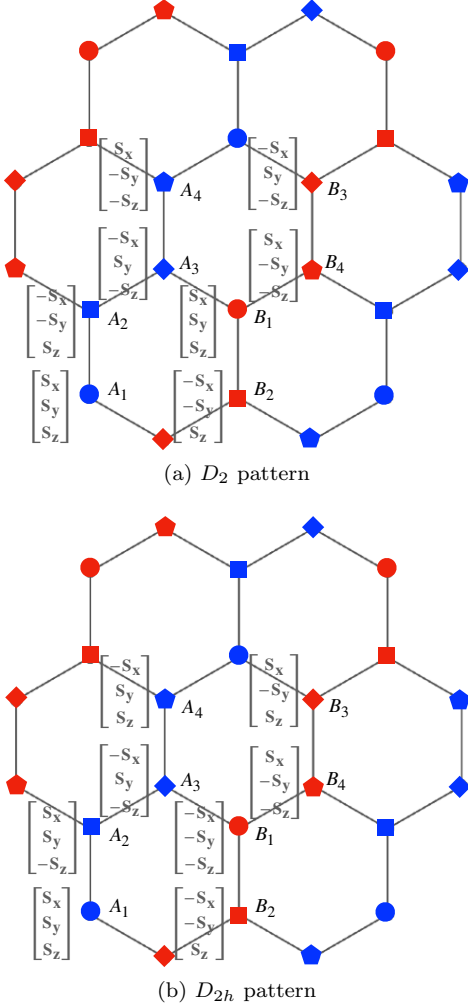


FIG. 6. Configurations of an arbitrary D_2 and D_{2h} state. The spin $\vec{S}_{A_1} = (S_x \ S_y \ S_z)^T$ is used as the reference spin, while orientations of other spins are determined according to the respective ordering matrices. Compared to stripy and zigzag orders, which are staggered arrangements of $\pm\vec{S}$, the sign flip in a D_2 and D_{2h} pattern can occur at individual components. In special cases $\vec{S}_{A_1} = (0 \ 0 \ \pm 1)^T$, these patterns are equivalent to the Z-type zigzag and stripy patterns in Figure 7, with a reduced four-site magnetic cell $\{A_1, A_2, A_3, B_3\}$. When choosing $\vec{S}_{A_1} = (\pm 1 \ 0 \ 0)^T$ and $(0 \ \pm 1 \ 0)^T$, X- and Y-type zigzag and stripy states will be realized, where the magnetic cell are given by $\{A_1, A_2, A_3, B_1\}$ and $\{A_2, A_3, B_1, B_2\}$, respectively. In general cases, the D_{2h} (D_2) and zigzag (stripy) orders are different, and the magnetic cell cannot be reduced to four sites.

gles. Since spins in those states are actually arranged according to the D_{2h} (D_2) pattern, the zigzag (stripy) moment of an individual sample is $\vec{m} = (0 \ 0 \ \cos\theta)^T$, and the corresponding ensemble average, by integrating over all allowed states, is $M = \frac{1}{4\pi} \int |\vec{m}| \sin\theta d\theta d\phi = \frac{1}{2}$. Hence, the D_{2h} and D_2 orders provide a more universal and complete description for the magnetization as compared to the zigzag and stripy order. (There is no phase

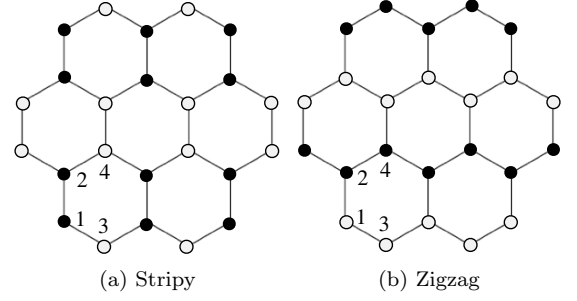


FIG. 7. Representative configurations of a stripy (ST) and zigzag (ZZ) order. White (\vec{S}) and black ($-\vec{S}$) cycles denote opposite spins. The corresponding magnetization can be defined as $M_{ST} = \langle |\frac{1}{N_{\text{cell}}} \sum_{\text{cell}} (\vec{S}_1 + \vec{S}_2 - \vec{S}_3 - \vec{S}_4)| \rangle$, and $M_{ZZ} = \langle |\frac{1}{N_{\text{cell}}} \sum_{\text{cell}} (\vec{S}_1 - \vec{S}_2 + \vec{S}_3 - \vec{S}_4)| \rangle$, respectively, where the numbers label the four sublattices. In general, \vec{S} may point to arbitrary directions. However, in the ground states of the Heisenberg-Kitaev model, the realization of these above configurations will be accompanied by $\vec{S} = (0 \ 0 \ \pm 1)^T$. We hence refer them as Z-type. Such states are present in the intersection of zigzag (stripy) and D_{2h} (D_2) manifolds.

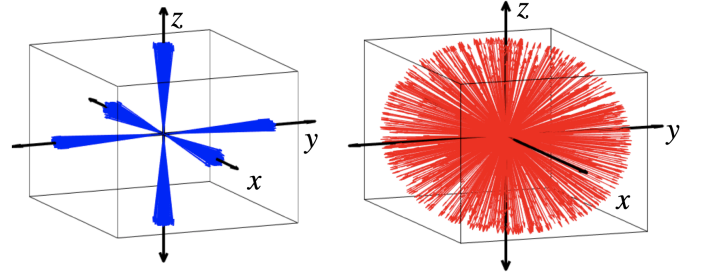


FIG. 8. Distribution of spin orientations for states in the ZZ/ D_{2h} and ST/ D_2 phases away (left) and at (right) the hidden $O(3)$ points, at a low temperature $T = 0.001$.

transition or crossover separating the $O(3)$ points from the neighboring points at $T \rightarrow 0$. For instance, it can be shown that the ground-state energy of the ZZ/ D_{2h} phase is $E = \frac{1}{3}(-K + J)$ per bond. This energy is degenerate with that of the Neel and FM order, $E_N = -\frac{1}{3}(K + J)$ and $E_{\text{FM}} = \frac{1}{3}(K + J)$, at $J = 0$ and $J = -K$, respectively, which are the two phase boundaries at $\varphi = \frac{\pi}{2}, \frac{3\pi}{4}$. Within the ZZ/ D_{2h} regime, the ground-state energy is linear to J/K . Nonetheless, TK-SVM is also capable of distinguishing states with continuous and discrete degeneracy; see Appendix C.)

V. HIDDEN $O(3)$ SYMMETRY

The D_2 and D_{2h} ordering matrices in Table I are a finite set of orthogonal matrices, which preserve the spin length and are invertible. This means that, by inverting those transformations, the D_2 and D_{2h} order can be

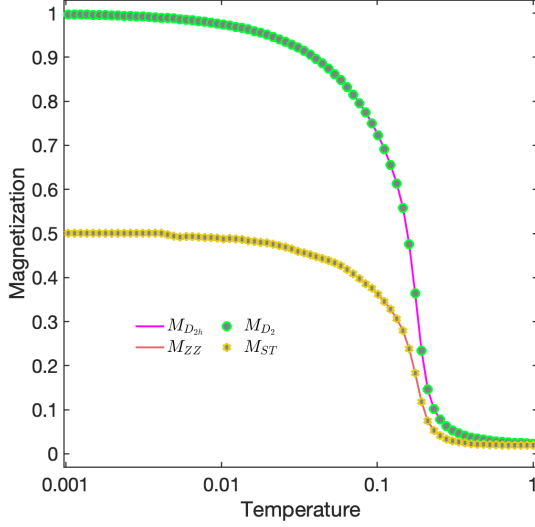


FIG. 9. Magnetization as a function of temperature at the $O(3)$ points, with $\varphi \approx 0.65\pi$ for the zigzag (ZZ) and D_{2h} orders and $\varphi \approx 1.65\pi$ for the stripy (ST) and D_2 orders. The D_{2h} (ZZ) and D_2 (ST) curves show the same behavior as the Heisenberg-Kitaev model is symmetric under a sub-lattice transformation $J \rightarrow -J, K \rightarrow -K$, and meanwhile $S_i \rightarrow -S_i$ for either of the honeycomb sublattices.

converted to simple ferromagnets.

Specifically, one can define \tilde{S} using a sublattice-dependent coordinate, $\tilde{S}_k = (T_k^{A,B})^T \tilde{S}$. The magnetization Eq. (4) then becomes $\vec{M} = \tilde{M} = \sum_k \tilde{S}_k$, describing a ferromagnetic alignment of \tilde{S} .

The above transformation acts on spin patterns. Naturally, one examines the form of the Hamiltonian in the same coordinate system. Without loss of generality, we focus on the interaction of a local bond $\langle kl \rangle_\gamma$, which can be rewritten as

$$H_{kl} = \vec{S}_k^T \hat{J}_\gamma \vec{S}_l, \quad (5)$$

where \hat{J}_γ has three possibilities depending on the type of the bond,

$$\begin{pmatrix} K+J & J \\ J & J \end{pmatrix}, \begin{pmatrix} J & K+J \\ J & J \end{pmatrix}, \begin{pmatrix} J & J \\ J & K+J \end{pmatrix}. \quad (6)$$

(Such expression can be easily generalized to other spin Hamiltonians.)

Under the sublattice-dependent coordinate transformations, Eq. (6) becomes

$$\tilde{H}_{kl} = \tilde{S}_k^T (\hat{T}_k^{A,B})^T \hat{J}_\gamma \hat{T}_l^{A,B} \tilde{S}_l. \quad (7)$$

The three different bonds transform as

$$\begin{aligned} \hat{J}_x &\rightarrow (\hat{T}_2^{A,B})^T \hat{J}_x \hat{T}_3^{A,B}, (\hat{T}_4^{A,B})^T \hat{J}_x \hat{T}_1^{A,B} \\ \hat{J}_y &\rightarrow (\hat{T}_{3(1)}^{A(B)})^T \hat{J}_y \hat{T}_{1(3)}^{B(A)}, (\hat{T}_{4(2)}^{A(B)})^T \hat{J}_y \hat{T}_{2(4)}^{B(A)} \\ \hat{J}_z &\rightarrow (\hat{T}_1^{A,B})^T \hat{J}_z \hat{T}_2^{A,B}, (\hat{T}_3^{A,B})^T \hat{J}_z \hat{T}_4^{A,B}, \end{aligned}$$

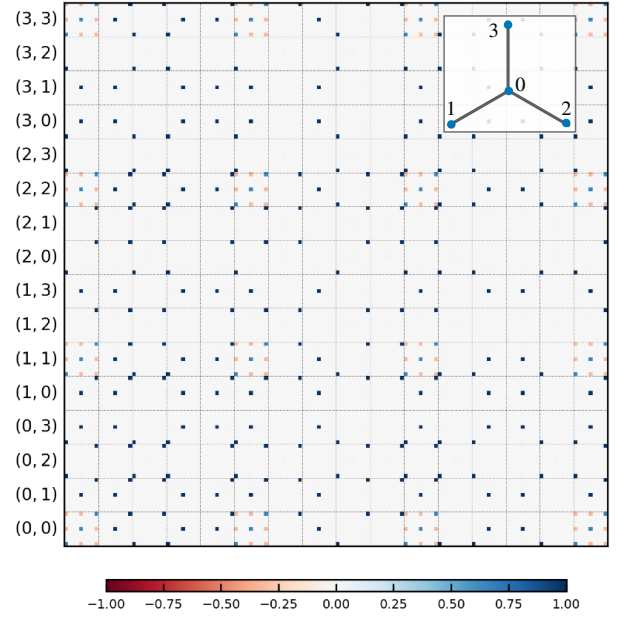


FIG. 10. The $C_{\mu\nu}$ matrix learned by a rank-2 TK-SVM with a four-spin triad cluster (inner panel) at the boundary point $\varphi = \frac{3\pi}{4}$. The axes iterate over spin indices (i, j) and spin components (α, β) in a lexicographically order, from bottom (left) to top (right). The spin indices divide the $C_{\mu\nu}$ matrix into 9×9 subblocks. Non-vanishing entries in a block represent the form of correlations between quadratic components $S_i^\alpha S_j^\beta$ and $S_{i'}^{\alpha'} S_{j'}^{\beta'}$. Blocks with $i = j$ and $i' = j'$ lead to constants owing to the trivial normalization $|\vec{S}| = 1$. Other blocks corresponds to the local constraints G_1 and G_2 . The pattern learned for $\varphi = \frac{7\pi}{4}$ (not shown) has a similar structure with sign flips in certain entries.

respectively leading to

$$\pm \begin{pmatrix} K+J & -J \\ -J & -J \end{pmatrix}, \pm \begin{pmatrix} -J & K+J \\ K+J & -J \end{pmatrix}, \pm \begin{pmatrix} -J & -J \\ -J & K+J \end{pmatrix}, \quad (8)$$

where “+” (“−”) corresponds to the D_2 (D_{2h}) order.

Clearly, at $K = -2J$, the couplings in the sublattice coordinate reduce to isotropic matrices, $\pm J \mathbb{1}$, where $\mathbb{1}$ denotes the identity matrix. \tilde{H}_{kl} is simply the local interaction for a ferromagnetic Heisenberg model of spin \tilde{S} , with $J > 0$ (< 0) in the D_2 (D_{2h}) phase. This precisely reproduces the hidden $O(3)$ symmetries of the HK model, which are previously identified in Ref. [32] by a dual transformation.

The above way of identifying hidden symmetries is especially straightforward. It does not use specific properties and hence does not rely on prior insights of a Hamiltonian. The high-symmetry points are self-evident once the order parameters are detected. Importantly, as shown in Figure 2 (c), data from the high-symmetry points are *not* needed in the training.

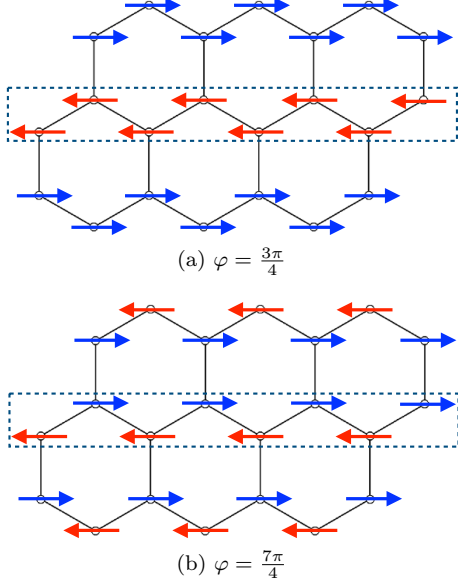


FIG. 11. Representative classical ground-state configuration at $\varphi = \frac{3\pi}{4}, \frac{7\pi}{4}$. The system forms ferromagnetic (a) or anti-ferromagnetic (b) Ising chains. The subdimensional symmetry leads to a classical subextensive degeneracy by flipping one entire chain of spins.

VI. LOCAL CONSTRAINTS AT PHASE BOUNDARIES

In general, at a phase boundary, the competition between the orders of the two phases can lead to more subtle properties such as an enhanced symmetry or an (emergent) local constraint. In this section we discuss the local constraints learned at the phase boundaries in the phase diagram of Figure 2. The cases $\varphi = \frac{\pi}{2}$ and $\varphi = \frac{3\pi}{2}$ correspond to pure Kitaev models and are not discussed here further because we already know from Ref. [45] that TK-SVM is able to learn the ground-state constraints for classical Kitaev spin liquids. We focus here therefore on the boundaries at $\varphi = \frac{3\pi}{4}$ and $\frac{7\pi}{4}$.

Learning local constraints follows the same procedure as learning magnetic orders but now a rank-2 TK-SVM able to detect quadratic correlations must be used. Figure 10 shows the $C_{\mu\nu}$ matrix for $\varphi = \frac{3\pi}{4}$. The pattern for $\varphi = \frac{7\pi}{4}$ has a similar structure but displays different signs for certain entries.

Two constraints, G_1 and G_2 , are inferred,

$$G_1 = \langle S_0^x(S_2^x + S_3^x) + S_0^y(S_1^y + S_3^y) + S_0^z(S_1^z + S_2^z) \rangle_{\text{td}} = \pm 2, \quad (9)$$

$$G_2 = \langle S_2^x S_3^x + S_1^x S_3^x + S_1^x S_2^x \rangle_{\text{td}} = 1, \quad (10)$$

with all other nearest neighbor and next-nearest neighbor correlations vanishing. Here, $\langle \cdot \rangle_{\text{td}}$ denotes a lattice average over triad clusters involving three bonds and four spins (see the inner panel of Figure 10), and “+”, “−” correspond to $\varphi = \frac{3\pi}{4}, \frac{7\pi}{4}$, respectively. These constraints

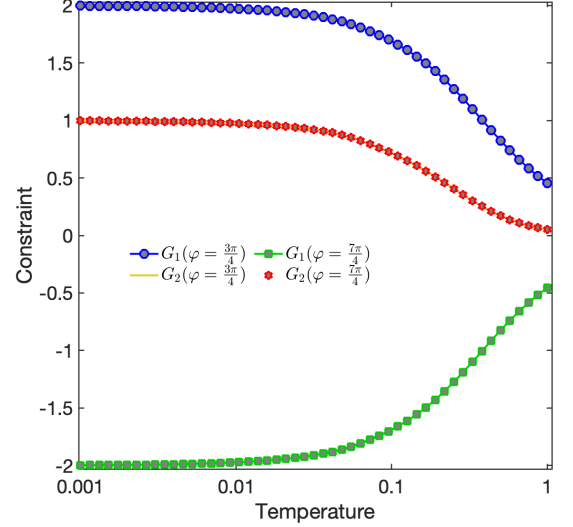


FIG. 12. Local constraints at $\varphi = \frac{3\pi}{4}, \frac{7\pi}{4}$ as a function of temperature. G_1 and G_2 satisfy Eqs. (9) and (10) in the ground state. (The G_2 curves at the two φ values overlap.)

are verified by their explicit measurement in a Monte Carlo simulation as shown in Figure 12.

The local constraints G_1 and G_2 are invariant under the following transformations,

$$S_0^x, S_2^x, S_3^x \rightarrow -S_0^x, -S_2^x, -S_3^x, \quad (11)$$

$$S_0^y, S_3^y, S_1^y \rightarrow -S_0^y, -S_3^y, -S_1^y, \quad (12)$$

$$S_0^z, S_1^z, S_2^z \rightarrow -S_0^z, -S_1^z, -S_2^z. \quad (13)$$

However, since a spin is shared by two triads, these do not define a local, but rather a *subdimensional* symmetry. For instance, Eq. (13) corresponds to a transformation flipping the S_z component of spins in a chain formed by x - and y -bonds, as depicted in Figure 11.

The solutions of Eqs.(9) and (10) give the classical ground states. The absence of cross terms, such as $S_i^\alpha S_j^{\beta \neq \alpha}$, indicates that each spin has only a single non-vanishing component in the ground state. To satisfy the two constraints, the system thereby forms ferromagnetic ($\varphi = \frac{3}{4}\pi$) and anti-ferromagnetic ($\varphi = \frac{7}{4}\pi$) Ising chains. Owing to the subdimensional symmetry, it does not cost energy to flip one Ising chain, leading to a subextensive line degeneracy with 3×2^L classical ground states. In other words, a \mathbb{Z}_2/D_{2h} (ST/ D_2) order is degenerate with a FM (Neel) order at these boundary points.

For the HK model at hand, this subextensive degeneracy will be lifted by quantum fluctuations via a quantum order-by-disorder mechanism [28, 33]. Nevertheless, from the point of view of machine learning, the above application implies a possibility of using machine-learning approaches to generate non-trivial spin models. The constraint G_1 is essential for the HK Hamiltonian at the classical phase boundaries where $J = -K$. However, during training, the Hamiltonian is *not* given to the machine but

rather learnt from the spin configurations by it. Hence training a specialized machine with symmetry-broken orders may also learn (new) models where competing orders can coexist, as in the case of spin liquids. We will leave this possibility for future work with a systematic investigation of the conditions on the stability of local and subdimensional degeneracies.

VII. SUMMARY AND OUTLOOK

In summary, we demonstrated that TK-SVM provides a data-driven approach to the problem of identifying hidden symmetries in phases with unconventional magnetic orders. In comparison with other constructions, which are typically contingent on the skill and experience of the researcher, this approach does not require particular knowledge of the Hamiltonian and is feasible even when prior insight in the system is limited.

We considered the honeycomb Heisenberg-Kitaev model as an example and successfully identified its hidden $O(3)$ points and the associated transformations. We also clarified that the D_{2h} and D_2 orders provide a more universal description of the magnetization compared to zigzag and stripy order. Our results emphasize the significance of being able to express the order parameter explicitly in many-body spin systems, which can be done by an interpretable machine-learning method like TK-SVM.

Moreover, we showed that our machine is also capable of revealing subdimensional symmetries. On the one hand, this complements our previous study of Ref. [45] which showed that TK-SVM identified the local Z_2 symmetry of classical Kitaev spin liquids by probing their ground-state constraints. On the other hand, as such symmetries are typically related to degenerate competing orders, their identification by machine learning methods implies a potential generative use of these machines in order to learn non-trivial spin models from symmetry-broken orders.

Hidden symmetries are also found in symmetry-protected topological states [55–57] such as the hidden $Z_2 \times Z_2$ symmetry in the celebrated Haldane phase [58–61]. The Haldane phase, as well as an array of other symmetry-protected topological states, can be mapped onto Landau-type orders by a nonlocal unitary transformation associated with the respective hidden symmetry [60–67]. How to detect such hidden symmetries with machine-learning techniques is an interesting topic left for future work. Even if it might be possible to construct an *ad hoc* machine for such a particular SPT phase, devising an expressive machine that is applicable to a (reasonably wide) class of topological phases remains however a very challenging task.

OPEN SOURCE AND DATA AVAILABILITY

The TK-SVM library has been made openly available with documentation and examples [68]. The data used in this work are available upon request.

ACKNOWLEDGMENTS

We thank Philippe Corboz, Matthias Gohlke, Jheng-Wei Li, Hao Song and Hong-Hao Tu for useful discussions. NR, KL, and LP acknowledge support from FP7/ERC Consolidator Grant QSIMCORR, No. 771891, and the Deutsche Forschungsgemeinschaft (DFG, German Research Foundation) under Germany’s Excellence Strategy – EXC-2111 – 390814868. Our simulations make use of the ν -SVM formulation [69], the LIBSVM library [70, 71], and the ALPSCore library [72].

Appendix A: Setting up of TK-SVM

Here we provide more details of TK-SVM and refer the reader to Refs. [40, 41] for the introduction of the method and Ref. [42] for a review, including comprehensive discussions on how to interpret $C_{\mu\nu}$ matrices.

The map ϕ in the decision function Eq. (2) maps a spin sample \mathbf{x} to a configuration of degree n monomials,

$$\phi : \mathbf{x} \rightarrow \phi(\mathbf{x}) = \{\phi_\mu\} = \{\langle S_{a_1}^{\alpha_1} \dots S_{a_n}^{\alpha_n} \rangle_{cl}\}, \quad (\text{A1})$$

where n also corresponds to the rank of a TK-SVM. This mapping partitions the system into clusters containing r spins labelled with $\alpha_n = \{1, 2, \dots, r\}$, while $\mu = \{\alpha_n, a_n\} = \{\alpha_1, a_1, \dots, \alpha_n, a_n\}$ denotes a collective index. ϕ is then averaged over the clusters, indicated by $\langle \dots \rangle_{cl}$, to reduce the dimension of the data. The optimal choice for the size and shape of the clusters is in general unknown *a priori*, and different phases in a phase diagram may have distinct translational symmetries. Therefore, in practice, we adopt clusters comprising a large number of lattice unit cells in order to accommodate diverse orders. In the results presented in the current work, clusters with a size up to 288 spins (12×12 honeycomb unit cells) were used.

The $C_{\mu\nu}$ matrix is defined by a weighted sum over support vectors,

$$C_{\mu\nu} = \sum_k \lambda_k \phi_\mu(\mathbf{x}^{(k)}) \phi_\nu(\mathbf{x}^{(k)}), \quad (\text{A2})$$

where λ_k is a Lagrange multiplier solved in the underlying SVM optimization problem, $\lambda_k \neq 0$ corresponds to a support vector. Non-vanishing entries of $C_{\mu\nu}$ represent correlations between particular monomial components.

Appendix B: Details of Graph Partitioning

For a binary classification between two sample sets “A” and “B”, the parameter ρ in decision function Eq. (2)

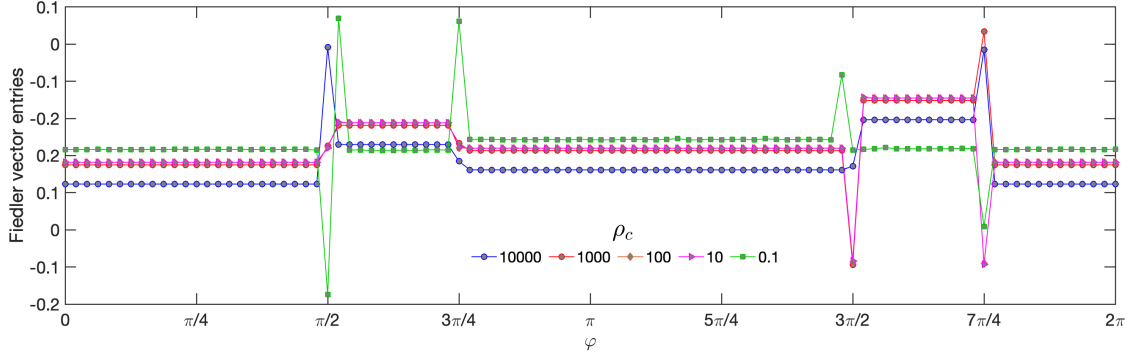


FIG. 13. Fiedler vectors obtained with different choices of ρ_c . In all cases, where ρ_c is large enough to set a characteristic scale “ $\gg 1$ ” for the reduced ρ criterion Eq. (B1), the clustering is evident and robust. The profound jumps at $\varphi = \frac{\pi}{2}, \frac{3\pi}{4}, \frac{3\pi}{2}, \frac{7\pi}{4}$ correspond to phase boundaries, as they do not belong to any plateaus (stable phases). A case of small $\rho_c = 0.1$ is also included for comparison. $\rho_c = 100$ is used in the maintext.

behaves as

$$|\rho_{AB}| \begin{cases} \gg 1 & \text{A, B in the same phase,} \\ \lesssim 1 & \text{A, B in different phases,} \end{cases} \quad (\text{B1})$$

which is referred as the reduced ρ criterion [41, 42].

The weight of an edge in the graph Figure 2a is determined by ρ in the decision function learned for the two end points, with a Lorentzian weighting function,

$$w(\rho) = 1 - \frac{\rho_c^2}{(|\rho| - 1)^2 + \rho_c^2} \in [0, 1), \quad (\text{B2})$$

where ρ_c is a super-parameter introduced to set a characteristic scale for “ $\gg 1$ ” in the above reduced ρ criterion. However, as we will discuss in Figure 13, the choice of ρ_c is not crucial.

The graph Figure 2a can be described by a Laplacian matrix,

$$\hat{L} = \hat{D} - \hat{A} = \begin{bmatrix} d_1 & -w_{12} & \dots & -w_{1M} \\ -w_{21} & d_2 & \dots & -w_{2M} \\ \vdots & & \ddots & \vdots \\ -w_{M1} & -w_{M2} & \dots & d_M \end{bmatrix}. \quad (\text{B3})$$

Here, the off-diagonal entries, $\omega_{ij} = \omega_{ji} = \omega(\rho_{ij})$, host all the edge weights and are collected by the adjacency matrix \hat{A} . The diagonal entries, $d_i = \sum_{j \neq i} \omega(\rho_{ij})$, represent degrees of the vertices and form the degree matrix \hat{D} . \hat{L} is symmetric by construction as only the magnitude of ρ is used. (The sign of ρ can reveal which data set is more disordered, but this property is not needed for the graph partitioning; see Refs. [41] and [42] for details.) According to Fiedler’s theory [46, 47], partitioning of a graph can be formulated as an eigenproblem of \hat{L} , as shown in Eq. (3). The second smallest eigenvector, known as the Fiedler vector, reflects the clustering of the graph.

In Figure 13, we compare the resultant Fiedler vectors using different values of ρ_c . The M vertices are classified into distinct subgraph components (indicated by the

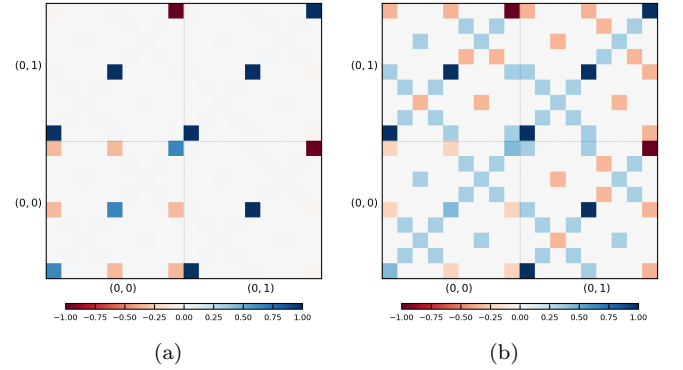


FIG. 14. Representative blocks of the $C_{\mu\nu}$ matrices of the ZZ/D_{2h} phase learned by a rank-2 TK-SVM with the eight-spin D_{2h} magnetic cell, away (a) and at (b) the $O(3)$ point. Blocks are labeled by the spin indices (i, j) . Non-vanishing entries in a block correspond to correlations between quadratic components $S_i^\alpha S_j^\beta$ and $S_{i'}^{\alpha'} S_{j'}^{\beta'}$. Negative elements in the $(0, 0)$ block reflect the spin normalization $|\vec{S}| = 1$. Non-trivial entries in (a) are the diagonal ones in each 9-by-9 subblock.

plateaus). In the case of $\rho_c = 0.1$, which does not suffice to define a scale “ $\gg 1$ ”, the partitioning is less obvious as all Fiedler-vector entries display very similar values. However, in all other cases, where ρ_c crosses several orders, the clustering is clear and robust.

Appendix C: Discriminating states in the same phase with different degeneracies

In Section IV we discussed that there is no singularity separating the high-symmetry points with a continuous $O(3)$ degeneracy from their neighboring points with a discrete three-fold degeneracy. Nevertheless, while they are thermodynamically in the same phase, those points can still be distinguished with the framework of TK-SVM.

This may be done by a rank-2 TK-SVM, as a magnetic order will also give finite quadratic correlations (which can be viewed as a “redundant” representation of the order parameter for the case at hand.) Results for the ZZ/D_{2h} phase are depicted in Figure 14 for instance. The rank-2 $C_{\mu\nu}$ pattern away from the high-symmetry point displays non-trivial quadratic correlations only the

diagonal elements in each subblock. The absent correlations between cross terms like $S_i^\alpha S_j^{\beta \neq \alpha}$ reflect locking of the spin orientation with a lattice axis, whereas such correlations are present in the pattern learned at the $O(3)$ point.

-
- [1] G. Carleo, I. Cirac, K. Cranmer, L. Daudet, M. Schuld, N. Tishby, L. Vogt-Maranto, and L. Zdeborová, *Rev. Mod. Phys.* **91**, 045002 (2019).
 - [2] J. Carrasquilla, *Advances in Physics: X* **5**, 1797528 (2020).
 - [3] L. Zdeborová and F. Krzakala, *Advances in Physics* **65**, 453 (2016).
 - [4] J. Sohl-Dickstein, E. A. Weiss, N. Maheswaranathan, and S. Ganguli, arXiv preprint arXiv:1503.03585 (2015).
 - [5] G. Carleo and M. Troyer, *Science* **355**, 602 (2017).
 - [6] L. Wang, *Phys. Rev. B* **94**, 195105 (2016).
 - [7] J. Carrasquilla and R. G. Melko, *Nat. Phys.* **13**, 431 (2017).
 - [8] Z. Nussinov, P. Ronhovde, D. Hu, S. Chakrabarty, B. Sun, N. A. Mauro, and K. K. Sahu, “Inference of hidden structures in complex physical systems by multi-scale clustering,” in *Information Science for Materials Discovery and Design*, edited by T. Lookman, F. J. Alexander, and K. Rajan (Springer International Publishing, Cham, 2016) pp. 115–138.
 - [9] K. T. Butler, D. W. Davies, H. Cartwright, O. Isayev, and A. Walsh, *Nature* **559**, 547 (2018).
 - [10] D. Morgan and R. Jacobs, *Annual Review of Materials Research* **50**, null (2020).
 - [11] D. Guest, K. Cranmer, and D. Whiteson, *Annual Review of Nuclear and Particle Science* **68**, 161 (2018).
 - [12] A. Radovic, M. Williams, D. Rousseau, M. Kagan, D. Bonacorsi, A. Himmel, A. Aurisano, K. Terao, and T. Wongjirad, *Nature* **560**, 41 (2018).
 - [13] M. Ntampaka, C. Avestruz, S. Boada, J. Caldeira, J. Cisewski-Kehe, R. Di Stefano, C. Dvorkin, A. E. Evrard, A. Farahi, D. Finkbeiner, *et al.*, arXiv preprint arXiv:1902.10159 (2019).
 - [14] M. Schuld and F. Petruccione, *Supervised Learning with Quantum Computers*, 1st ed. (Springer Publishing Company, Incorporated, 2018).
 - [15] J. Biamonte, P. Wittek, N. Pancotti, P. Rebentrost, N. Wiebe, and S. Lloyd, *Nature* **549**, 195 (2017).
 - [16] J. Haah, A. W. Harrow, Z. Ji, X. Wu, and N. Yu, *IEEE Transactions on Information Theory* **63**, 5628 (2017).
 - [17] D. Luo and B. K. Clark, *Phys. Rev. Lett.* **122**, 226401 (2019).
 - [18] D. Pfau, J. S. Spencer, A. G. d. G. Matthews, and W. M. C. Foulkes, arXiv preprint arXiv:1909.02487 (2019).
 - [19] J. Hermann, Z. Schätzle, and F. Noé, arXiv preprint arXiv:1909.08423 (2019).
 - [20] H.-J. Liao, J.-G. Liu, L. Wang, and T. Xiang, *Phys. Rev. X* **9**, 031041 (2019).
 - [21] G. Carleo, K. Choo, D. Hofmann, J. E. Smith, T. Westerhout, F. Alet, E. J. Davis, S. Efthymiou, I. Glasser, S.-H. Lin, M. Mauri, G. Mazzola, C. B. Mendl, E. van Nieuwenburg, O. O’Reilly, H. Théveniaut, G. Torlai, F. Vicentini, and A. Wietek, *SoftwareX* **10**, 100311 (2019).
 - [22] Y. Nagai, H. Shen, Y. Qi, J. Liu, and L. Fu, *Phys. Rev. B* **96**, 161102 (2017).
 - [23] Y. Zhang, A. Mesaros, K. Fujita, S. D. Edkins, M. H. Hamidian, K. Ch’ng, H. Eisaki, S. Uchida, J. C. S. Davis, E. Khatami, and E.-A. Kim, *Nature* **570**, 484 (2019).
 - [24] G. Torlai, B. Timar, E. P. L. van Nieuwenburg, H. Levine, A. Omran, A. Keesling, H. Bernien, M. Greiner, V. Vuletić, M. D. Lukin, R. G. Melko, and M. Endres, *Phys. Rev. Lett.* **123**, 230504 (2019).
 - [25] A. Bohrdt, C. S. Chiu, G. Ji, M. Xu, D. Greif, M. Greiner, E. Demler, F. Grusdt, and M. Knap, *Nature Physics* **15**, 921 (2019).
 - [26] A. Kitaev, *Ann. Phys. (N. Y.)* **321**, 2 (2006), january Special Issue.
 - [27] G. Jackeli and G. Khaliullin, *Phys. Rev. Lett.* **102**, 017205 (2009).
 - [28] J. Chaloupka, G. Jackeli, and G. Khaliullin, *Phys. Rev. Lett.* **105**, 027204 (2010).
 - [29] H. Takagi, T. Takayama, G. Jackeli, G. Khaliullin, and S. E. Nagler, *Nat. Rev. Phys.* **1**, 264 (2019).
 - [30] L. Janssen and M. Vojta, *J. Phys.: Condens. Matter* **31**, 423002 (2019).
 - [31] S. M. Winter, A. A. Tsirlin, M. Daghofer, J. van den Brink, Y. Singh, P. Gegenwart, and R. Valentí, *Journal of Physics: Condensed Matter* **29**, 493002 (2017).
 - [32] J. Chaloupka and G. Khaliullin, *Phys. Rev. B* **92**, 024413 (2015).
 - [33] J. Chaloupka, G. Jackeli, and G. Khaliullin, *Phys. Rev. Lett.* **110**, 097204 (2013).
 - [34] J. Rusnačko, D. Gotfryd, and J. Chaloupka, *Phys. Rev. B* **99**, 064425 (2019).
 - [35] G. Uimin, *JETPL* **12**, 225 (1970).
 - [36] C. K. Lai, *Journal of Mathematical Physics* **15**, 1675 (1974).
 - [37] B. Sutherland, *Phys. Rev. B* **12**, 3795 (1975).
 - [38] C. D. Batista, G. Ortiz, and J. E. Gubernatis, *Phys. Rev. B* **65**, 180402 (2002).
 - [39] B. Zhao, P. Weinberg, and A. W. Sandvik, *Nature Physics* **15**, 678 (2019).
 - [40] J. Greitemann, K. Liu, and L. Pollet, *Phys. Rev. B* **99**, 060404(R) (2019).
 - [41] K. Liu, J. Greitemann, and L. Pollet, *Phys. Rev. B* **99**, 104410 (2019).
 - [42] J. Greitemann, K. Liu, L. D. C. Jaubert, H. Yan, N. Shannon, and L. Pollet, *Phys. Rev. B* **100**, 174408 (2019).
 - [43] C. Price and N. B. Perkins, *Phys. Rev. B* **88**, 024410 (2013).

- [44] L. Janssen, E. C. Andrade, and M. Vojta, *Phys. Rev. Lett.* **117**, 277202 (2016).
- [45] K. Liu, N. Sadoune, N. Rao, J. Greitemann, and L. Pollet, arXiv preprint arXiv:2004.14415 (2020).
- [46] M. Fiedler, *Czechoslovak Mathematical Journal* **23**, 298 (1973).
- [47] M. Fiedler, *Czechoslovak Mathematical Journal* **25**, 619 (1975).
- [48] J. Osorio Iregui, P. Corboz, and M. Troyer, *Phys. Rev. B* **90**, 195102 (2014).
- [49] M. Gohlke, R. Verresen, R. Moessner, and F. Pollmann, *Phys. Rev. Lett.* **119**, 157203 (2017).
- [50] J. Wang, B. Normand, and Z.-X. Liu, *Phys. Rev. Lett.* **123**, 197201 (2019).
- [51] X.-Y. Dong and D. Sheng, arXiv preprint arXiv:1911.12854 (2019).
- [52] G. Khaliullin and S. Okamoto, *Phys. Rev. Lett.* **89**, 167201 (2002).
- [53] G. Khaliullin, *Progress of Theoretical Physics Supplement* **160**, 155 (2005).
- [54] C. C. Price and N. B. Perkins, *Phys. Rev. Lett.* **109**, 187201 (2012).
- [55] Z.-C. Gu and X.-G. Wen, *Phys. Rev. B* **80**, 155131 (2009).
- [56] X. Chen, Z.-C. Gu, and X.-G. Wen, *Phys. Rev. B* **83**, 035107 (2011).
- [57] F. Pollmann, E. Berg, A. M. Turner, and M. Oshikawa, *Phys. Rev. B* **85**, 075125 (2012).
- [58] I. Affleck, T. Kennedy, E. H. Lieb, and H. Tasaki, *Phys. Rev. Lett.* **59**, 799 (1987).
- [59] I. Affleck, T. Kennedy, E. H. Lieb, and H. Tasaki, *Communications in Mathematical Physics* **115**, 477 (1988).
- [60] T. Kennedy and H. Tasaki, *Phys. Rev. B* **45**, 304 (1992).
- [61] T. Kennedy and H. Tasaki, *Communications in Mathematical Physics* **147**, 431 (1992).
- [62] M. den Nijs and K. Rommelse, *Phys. Rev. B* **40**, 4709 (1989).
- [63] H.-H. Tu, G.-M. Zhang, and T. Xiang, *Phys. Rev. B* **78**, 094404 (2008).
- [64] H.-H. Tu, G.-M. Zhang, and T. Xiang, *Journal of Physics A: Mathematical and Theoretical* **41**, 415201 (2008).
- [65] H.-H. Tu, G.-M. Zhang, T. Xiang, Z.-X. Liu, and T.-K. Ng, *Phys. Rev. B* **80**, 014401 (2009).
- [66] D. V. Else, S. D. Bartlett, and A. C. Doherty, *Phys. Rev. B* **88**, 085114 (2013).
- [67] K. Duivenvoorden and T. Quella, *Phys. Rev. B* **88**, 125115 (2013).
- [68] J. Greitemann, K. Liu, and L. Pollet, tensorial-kernel SVM library, <https://gitlab.physik.uni-muenchen.de/tk-svm/tksvm-op>.
- [69] B. Schölkopf, A. J. Smola, R. C. Williamson, and P. L. Bartlett, *Neural Comput.* **12**, 1207 (2000).
- [70] C.-C. Chang and C.-J. Lin, *Neural Comput.* **13**, 2119 (2001).
- [71] C.-C. Chang and C.-J. Lin, *ACM Trans. Intell. Syst. Technol.* **2**, 27:1 (2011).
- [72] A. Gaenko, A. Antipov, G. Carcassi, T. Chen, X. Chen, Q. Dong, L. Gamper, J. Gukelberger, R. Igarashi, S. Isakov, M. Könz, J. LeBlanc, R. Levy, P. Ma, J. Paki, H. Shinaoka, S. Todo, M. Troyer, and E. Gull, *Comput. Phys. Commun.* **213**, 235 (2017).